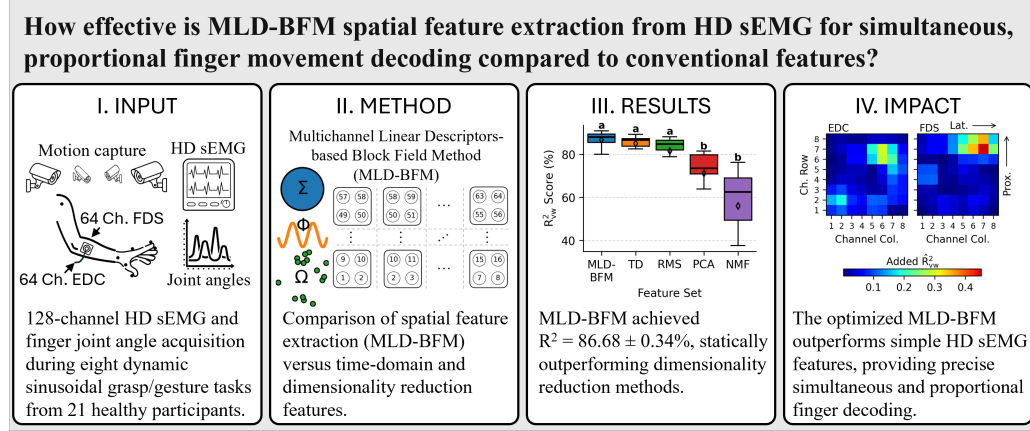


# Graphical Abstract

## Simultaneous and Proportional Finger Motion Decoding Using Spatial Features from High-Density Surface Electromyography

Ricardo Gonçalves Molinari, Leonardo Abdala Elias



## Highlights

### **Simultaneous and Proportional Finger Motion Decoding Using Spatial Features from High-Density Surface Electromyography**

Ricardo Gonçalves Molinari, Leonardo Abdala Elias

- The spatial features from high-density surface electromyography were evaluated.
- It achieved 86.7% accuracy in simultaneous and proportional finger decoding.
- Optimal feature hyperparameters:  $2 \times 2$  spatial block and 0.15-second window.
- The new spatial-feature method outperformed dimensionality-reduction approaches.
- Informative muscle-activity regions mapped to proximal-lateral electrode array zones.

# Simultaneous and Proportional Finger Motion Decoding Using Spatial Features from High-Density Surface Electromyography

Ricardo Gonçalves Molinari<sup>a</sup>, Leonardo Abdala Elias<sup>a,b,\*</sup>

<sup>a</sup>*Neural Engineering Research Laboratory, Center for Biomedical Engineering, University of Campinas, Cidade Universitária Zeferino Vaz, Campinas, 13083-881, SP, Brazil*

<sup>b</sup>*Department of Electronics and Biomedical Engineering, School of Electrical and Computer Engineering, University of Campinas, Cidade Universitária Zeferino Vaz, Campinas, 13083-852, SP, Brazil*

---

## Abstract

Restoring natural and intuitive hand function requires simultaneous and proportional control (SPC) of multiple degrees of freedom (DoFs). This study systematically evaluated the multichannel linear descriptors-based block field method (MLD-BFM) for continuous decoding of five finger-joint DoFs by leveraging the rich spatial information of high-density surface electromyography (HD sEMG). Twenty-one healthy participants performed dynamic sinusoidal finger movements while HD sEMG signals were recorded from the *extensor digitorum communis* (EDC) and *flexor digitorum superficialis* (FDS) muscles. MLD-BFM extracted region-specific spatial features, including effective field strength ( $\Sigma$ ), field-strength variation rate ( $\Phi$ ), and spatial complexity ( $\Omega$ ). Model performance was optimized (block size:  $2 \times 2$ ; window: 0.15 s) and compared with conventional time-domain features and dimensionality reduction approaches when applied to multi-output regression models. MLD-BFM consistently achieved the highest  $R_{vw}^2$  values across all models. The multilayer perceptron (MLP) combined with MLD-BFM yielded the best performance ( $R_{vw}^2 = 86.68\% \pm 0.33$ ). Time-domain features also showed strong predictive capability and were statistically comparable to MLD-BFM in some models, whereas dimensionality reduction techniques exhibited lower accuracy. Decoding accuracy was higher for the middle and ring fingers than for the thumb. Overall, MLD-BFM improved continuous

---

\*Corresponding author: leoelias@unicamp.br

finger movement decoding accuracy, underscoring the importance of taking advantage of the spatial richness of HD sEMG. These findings suggest that spatially structured features enhance SPC and provide practical guidance for designing robust, real-time, and responsive myoelectric interfaces.

*Keywords:* High-Density Surface Electromyography (HD sEMG), Multichannel Linear Descriptors based Block Field Method (MLD-BFM), Finger Kinematics, Prosthetic Control, Simultaneous and Proportional Control

---

## 1. Introduction

Restoring natural and intuitive hand function in individuals with impaired hand motor function using controlled upper-limb prostheses remains a major challenge in neurorehabilitation engineering [1, 2]. Surface electromyography (sEMG) is the most widely adopted non-invasive interface for prosthetic control [3], capturing the electrical signals generated by muscle fibers under neural command. While pattern recognition-based control (PRC) successfully classifies discrete hand gestures with high accuracy, natural and continuous volitional prosthetic control, or simultaneous and proportional control (SPC) across multiple degrees of freedom (DoFs), involves a far more complex problem [4].

Regression-based approaches have been extensively explored to bridge this gap, aiming to map sEMG signals to continuous kinematic outputs. Seminal work by [5] demonstrated the feasibility of predicting multiple hand and wrist DoFs using multilayer perceptrons (MLP). Subsequent studies investigated a variety of models, including kernel ridge regression [6], support vector machines [7], k-nearest neighbors (KNN) [8], and ridge regression [9]. These methods predominantly relied on time-domain features (e.g., root mean square - RMS, mean absolute value - MAV, waveform length - WL). Although promising, these conventional features may not fully exploit the rich spatial information provided by high-density sEMG (HD sEMG) arrays, which can limit their ability to decode the subtle and coordinated muscle activation patterns underlying dexterous hand movements.

The advent of HD sEMG has significantly advanced the study of muscular activity by enabling higher spatial resolution recordings. Unlike conventional sparse electrode arrays, HD sEMG captures detailed topographic information that researchers can use to disentangle complex motor commands [10]. By

leveraging the spatial distribution of muscle activation patterns, HD sEMG allows a more precise characterization of the spatial organization and coordination of muscle activity during dynamic tasks.

The multichannel linear descriptors (MLD) framework, originally developed to describe global functional states in electroencephalography (EEG) [11, 12, 13], was recently adapted to HD sEMG to exploit its rich spatial information [14]. The MLD quantifies three global spatial properties within defined regions of interest. The effective field strength ( $\Sigma$ ) captures the overall intensity of muscle activation, the field strength variation rate ( $\Phi$ ) reflects the speed of spatial field changes during dynamic contractions, and the measure of spatial complexity ( $\Omega$ ) reflects the diversity of activity across different generators, serving as a quantification of the number of relevant sources [15]. Building on this framework, Peng et al. [14] proposed the multichannel linear descriptors-based block field method (MLD-BFM), which extracts MLD features from local electrode blocks and substantially improves pattern recognition accuracy for multiple hand and wrist movements. Although MLD-BFM has demonstrated strong performance in classification tasks, its potential to enhance continuous, simultaneous, and proportional regression of finger movements has not yet been fully explored.

In this study, we provide a systematic evaluation of the MLD-BFM feature extraction method for continuous and proportional decoding of finger movements across five DoFs, and compare its performance with commonly used feature sets, including RMS, the combination of MAV and WL (MAV-WL), and dimensionality-reduced representations such as PCA and NMF. The results indicate that, while MLD-BFM did not show statistically significant differences compared to MAV-WL and RMS, it consistently achieved higher average performance across all tested regressor models. By capturing the spatial distribution of muscle activity, MLD-BFM provided a more informative input for regression models. Across linear, nonlinear, and instance-based regressors, MLD-BFM outperformed the alternative feature sets in terms of mean accuracy, thereby enhancing motion intention estimation. These findings highlight the advantages of spatially structured features for SPC and provide insights that may guide the development of myoelectric control systems toward more natural, responsive, and clinically relevant implementations.

## 2. Materials and Methods

### 2.1. Participants

Twenty-one healthy participants, including 10 women and 11 men, completed the experimental protocol. The age was  $27.19 \pm 6.55$  years, body weight was  $73.52 \pm 16.06$  kg, and height was  $1.68 \pm 0.11$  m. One participant was left-handed. None of the participants reported neuromusculoskeletal disorders affecting the dominant hand. The Research Ethics Committee of the University of Campinas approved the study (CAAE 59961616.8.0000.5404) on 24 October 2024, and all participants provided informed consent before the experiments.

### 2.2. Experimental Protocol

Participants followed instructions to replicate dynamic, sinusoidal finger movements displayed by a virtual hand model on a custom interface, which was displayed on a monitor placed in front of the participant while they were seated comfortably with their elbow resting on a height-adjustable table (Fig. 1A). Tasks began with the fingers fully extended, followed by eight movement patterns: flexion/extension (F/E) of the index finger; F/E of the middle finger; F/E of ring and little fingers simultaneously; thumb opposition and retraction; pinch grasp and release with the index finger and thumb; pinch with the middle finger and thumb; tripod pinch with the index, middle, and thumb; and 5-finger grasping. Sinusoidal movements were displayed at 0.50 Hz and 0.75 Hz, yielding 16 trials per set. Each participant completed three sets of trials, totaling 48 tasks. The order of the tasks within each set was randomized to minimize sequence effects. In the present study, only the 0.50 Hz tasks from the first set were used, as they provided sufficient data for evaluating continuous and proportional decoding while reducing potential confounding effects related to fatigue, movement speed, and potential motor learning processes. Each task lasted 45 seconds, with at least 30 seconds of rest between tasks.

### 2.3. Data Acquisition

HD sEMG signals were recorded using a custom acquisition and processing platform described previously [16]. The system consisted of two 64-channel electrophysiological acquisition devices (RHD2164, Intan Technologies, USA), totaling 128 channels, with a sampling rate of 2052.52 Hz

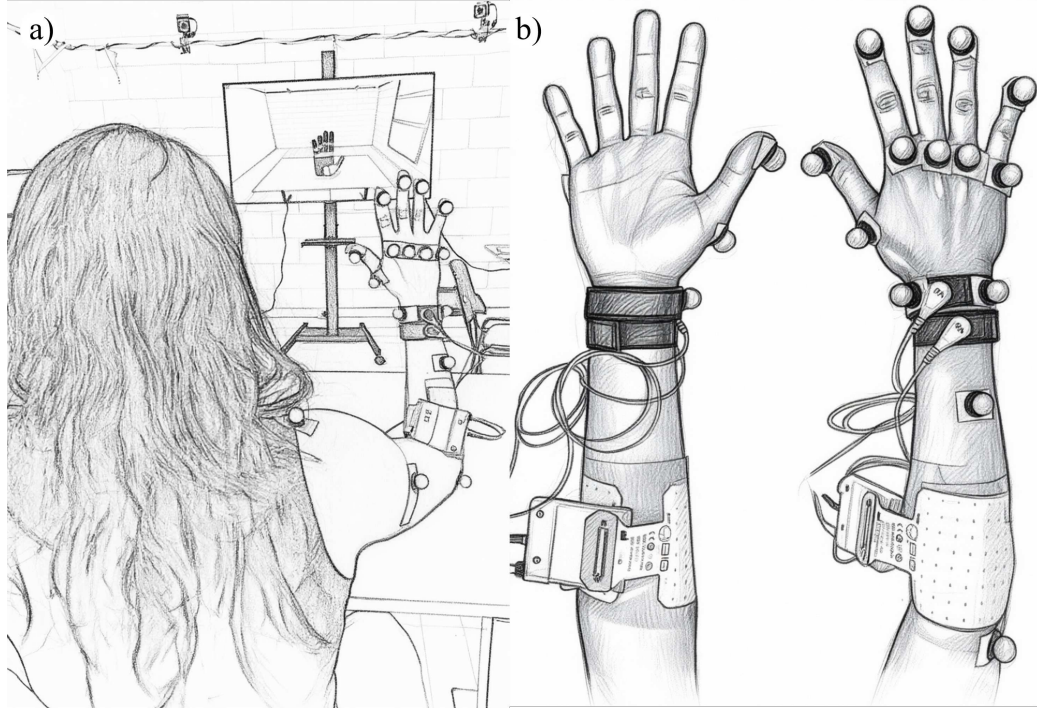


Figure 1: a) Experimental setup for the synchronous repetition of dynamic movements following a sinusoidal pattern. The finger position for all tasks was visually displayed on the screen in front of the participant. b) illustrates the positioning of the electrode arrays over the extensor digitorum communis (EDC) and flexor digitorum superficialis (FDS) muscles, as well as the reflective markers used in the motion capture system.

per channel. Two 64-channel electrode arrays (GR10MM0808, OT Bioelettronica, Italy) were placed over the Extensor Digitorum Communis (EDC) and the Flexor Digitorum Superficialis (FDS) [17], following skin abrasion with an exfoliating paste and cleaning with 70% alcohol (Fig. 1B). Reference electrodes were attached to the wrist using water-moistened conductive straps. During acquisition, signals were filtered through third-order analog Butterworth bandpass filters (10–500 Hz). The platform synchronized the start of HD sEMG recordings with the custom interface and the Vicon Vero 2.2 motion capture system (Vicon Motion Systems, UK), which operated at a frequency of 100 Hz. The kinematic data were processed using a biomechanical hand model to estimate finger joint angles.

## 2.4. Block Field Method (BFM)

The block field method (BFM) offers a structured approach to extracting spatial descriptors from HD sEMG signals by partitioning the electrode grid into local regions and computing features within each block. This approach enables the analysis of spatial activation patterns at different scales while balancing spatial resolution and computational cost.

Let  $X \in \mathbb{R}^{S \times C}$  denote the filtered HD sEMG signal matrix, with  $S$  samples and  $C = n_{\text{rows}} \cdot n_{\text{cols}}$  channels recorded from an  $8 \times 8$  electrode grid (i.e.,  $n_{\text{rows}} = n_{\text{cols}} = 8$ ). The electrode grid was segmented into spatial blocks of size  $B \times B$  channels, where  $B$  can range from 1 to 8, forming  $K = B^2$  channels per block (Fig. 2).

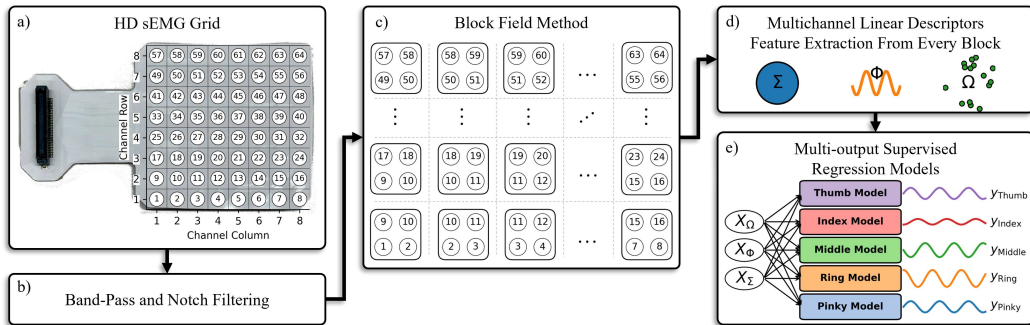


Figure 2: Schematic representation of the signal processing and feature extraction pipeline: a) electrode grid channels arranged in rows and columns; b) band-pass and notch filtering; c) block field method (BFM) example with  $2 \times 2$  blocks and unit step; d) extraction of effective field strength ( $\Sigma$ ), field strength variation rate ( $\Phi$ ), and spatial complexity ( $\Omega$ ); and e) multi-output supervised regression model.

The block size  $B$  determines the spatial extent of each feature descriptor: smaller blocks capture finer spatial details and local variations of the HD sEMG signals, but result in a larger number of blocks  $n_B$  and higher computational cost. Conversely, larger blocks provide a more global representation by aggregating signals over a wider area, reducing the total number of blocks and computational load, but potentially smoothing out finer spatial information.

In addition to the block size, the step parameter  $e$  defines how the  $B \times B$  blocks were distributed across the electrode grid. Specifically,  $e$  determines the spatial displacement between consecutive blocks along both the row and column directions, effectively controlling the spatial sampling of the block

across the electrode grid. The total number of blocks,  $n_B$ , was determined by the number of rows  $n_{\text{rows}}$  and columns  $n_{\text{cols}}$ , and the block parameters  $B$  and  $e$  (Eq. 1). Unlike the original implementation of the method [14], where the two lateral sides of the unfolded electrode grid were connected on the forearm, allowing blocks to slide across the lateral boundaries, in the present study, the grid was not wrapped, and therefore block placement was restricted to within the physical boundaries of each array.

$$n_B = \left( \left\lfloor \frac{n_{\text{rows}} - B}{e} \right\rfloor + 1 \right) \cdot \left( \left\lfloor \frac{n_{\text{cols}} - B}{e} \right\rfloor + 1 \right) \quad (1)$$

In addition to the spatial configuration defined by the block size and step, temporal segmentation plays a key role in determining the resolution of the extracted features. Temporal windows of  $L$  consecutive samples with overlap  $O$  were defined to segment the signal in time, allowing the extraction of descriptors from short, quasi-stationary segments of the HD sEMG signals. For a given block  $b$ , the  $w$ -th temporal window restricted to the channels of the block was given by Eq. 2, where  $\mathcal{I}_b \subset \{1, \dots, C\}$  denotes the set of indices corresponding to the  $K = B^2$  channels of block  $b$ . Accordingly, we define  $X_{w,b} \in \mathbb{R}^{L \times K}$  as the segment of the HD sEMG signals corresponding to window  $w$  and block  $b$ .

$$X_{w,b} = X[t_w : t_w + L, \mathcal{I}_b], \quad t_w = w \cdot (L - O), \quad w = 0, \dots, W - 1 \quad (2)$$

The window length determines the temporal extent of each segment and thus the temporal resolution of the extracted descriptors: shorter windows capture fast temporal variations and transient signal dynamics but may be more sensitive to noise, whereas longer windows provide smoother, less variable estimates at the expense of temporal precision. The overlap  $O$  allows consecutive windows to share data, increasing temporal continuity and reducing abrupt changes between windows. The number of temporal windows  $W$  was determined by Eq. 3. Together with the spatial block size  $B$  and step  $e$ , the window length  $L$  and overlap  $O$  define the spatiotemporal resolution and coverage of the features extracted from the HD sEMG signals.

$$W = \left\lfloor \frac{N - L}{L - O} \right\rfloor + 1 \quad (3)$$

### 2.5. Multichannel Linear Descriptors (MLD)

Researchers originally developed the multichannel linear descriptors (MLD) framework for multichannel EEG analysis as a linear and physically interpretable method to describe global functional brain states [12, 13]. The framework summarizes the spatial distribution of multichannel signals through a compact set of descriptors with clear physical meaning, providing an efficient representation of spatial information. The present study adapts the MLD framework to HD sEMG to characterize muscle activation patterns. The multichannel linear descriptors-based block field method (MLD-BFM) segments the electrode grid into spatial regions and extracts MLD features from each block [14], enabling a structured and localized description of the spatial organization of muscular activity associated with different hand movements.

To formalize the feature computation, the analysis represents the HD sEMG signals in matrix form. The matrix  $X_{w,b} \in \mathbb{R}^{L \times K}$  describes the spatiotemporal segment associated with block  $b$  during temporal window  $w$ , where  $K = B^2$  denotes the number of channels within the block and  $L$  represents the number of temporal samples. Each entry  $X_{w,b}(t, k)$  contains the signal value at the  $t$ -th time index ( $1 \leq t \leq L$ ) and the  $k$ -th channel ( $1 \leq k \leq K$ ) in this segment.

The first descriptor, the *effective field strength* ( $\Sigma$ ), was originally developed to characterize the global field strength and quantifies the overall intensity of the electrical field, serving as the multidimensional analogue of Hjorth's activity descriptor [18]. The squared value  $\Sigma^2$  corresponds to the mean integral power per channel. In HD sEMG,  $\Sigma$  serves as a spatial descriptor of muscle activation patterns across different regions, analogous to the root mean square (RMS) amplitude of the signals, which provides sensitivity to contraction strength. More specifically,  $\Sigma$  represents the field power within a spatial block and quantifies the intensity of muscle activity beneath the corresponding electrode region. The formal definition of  $\Sigma$  was provided in Eq. 4.

$$\Sigma_{w,b} = \sqrt{\frac{1}{KL} \sum_{t=1}^L \sum_{k=1}^K X_{w,b}(t, k)^2} \quad (4)$$

The second descriptor, the *field strength variation rate* ( $\Phi$ ), was originally used to describe the speed of state transitions in brain electrical activity and

can be interpreted as the number of rotations per second in state space [12]. In HD sEMG,  $\Phi$  quantifies the dominant rate of change of the muscle electric field within a spatial block, serving as a generalized frequency measure (units of  $s^{-1}$  or Hz) that captures the temporal dynamics of muscle activity recorded by multiple electrodes in a localized region. The mathematical definition of  $\Phi$  was provided in Eq. 5, where  $f_s$  denotes the sampling frequency.

$$\Phi_{w,b} = \frac{1}{2\pi} \sqrt{\frac{\sum_{t=1}^{L-1} \sum_{k=1}^K \left( \frac{X_{w,b}(t+1,k) - X_{w,b}(t,k)}{\Delta t} \right)^2}{\sum_{t=1}^L \sum_{k=1}^K X_{w,b}(t, k)^2}}, \quad \Delta t = \frac{1}{f_s} \quad (5)$$

The third descriptor, *spatial complexity* ( $\Omega$ ), was originally developed to quantify the diversity of underlying sources in EEG data and to provide a comprehensive characterization of global functional brain states [11]. In its original formulation,  $\Omega$  was derived from the normalized eigenvalues of the covariance matrix, capturing the geometrical complexity of the data in state space. The value of  $\Omega$  represents the effective number of relevant sources required to describe the spatial structure of the signals [13].  $\Omega$  ranges from 1 to  $K$ : it equals 1 when the data contain exactly one spatial mode, with the total variance concentrated in a single dimension, and it equals  $K$  when the total variance was uniformly distributed across all  $K$  modes, indicating distributed and heterogeneous activation [15]. In HD sEMG,  $\Omega$  serves as a spatial feature that characterizes muscle activation patterns within electrode blocks, following the same interpretation used in EEG.

The computation of  $\Omega$  involves three main steps. First, the covariance matrix  $C_{w,b}$  of the block signals was calculated as shown in Eq. 6, where the product  $X_{w,b}^\top X_{w,b}$  captures the correlation structure among channels within each block. Second, the eigenvalues of this covariance matrix were normalized according to Eq. 7, yielding  $\tilde{\lambda}_i$ , which define a probability distribution over spatial modes of variance. Finally,  $\Omega_{w,b}$  was obtained as the entropy-like measure defined in Eq. 8, quantifying the degree of spatial complexity.

$$C_{w,b} = \frac{1}{L} X_{w,b}^\top X_{w,b}, \quad (6)$$

$$\tilde{\lambda}_i = \frac{\lambda_i(C_{w,b})}{\sum_{j=1}^K \lambda_j(C_{w,b})}, \quad (7)$$

$$\Omega_{w,b} = \exp \left( - \sum_{i=1}^K \tilde{\lambda}_i \log \tilde{\lambda}_i \right) \quad (8)$$

### 2.6. Data Processing

Feature and target matrices were generated from raw HD sEMG and finger joint angle signals, respectively, for model training and testing. The HD sEMG signals were processed using zero-phase fourth-order Butterworth bandpass filtering (10–500 Hz) and a 60 Hz notch filter with a quality factor of 30. Each task was cropped to retain data between 4 and 44 seconds, removing transient segments at the beginning and end of each motor task. Spatial features were then extracted from the filtered signals using the MLD-BFM method, and the finger joint angles were resampled to match the temporal resolution of the HD sEMG feature set.

For each task, the data were split into training and test sets with a fixed proportion of 0.5, without shuffling, to preserve the temporal structure. Feature and target matrices from all tasks were concatenated to form complete training and test datasets. The training data were then randomly permuted to improve model generalization, whereas the test data remained in sequential order to maintain temporal structure for visualization and performance evaluation.

### 2.7. Regression Models

A pool of multi-output regression models was implemented to learn the mapping between HD sEMG features and finger joint angles. Each model operated within a standardized regression framework that applied input standardization and joint-output normalization, scaling all finger angles simultaneously to preserve inter-output amplitude relationships and stabilize multi-output training. Predicted trajectories were post-processed using a zero-phase fourth-order Butterworth low-pass filter with a cutoff frequency of 5 Hz.

The model pool included multilayer perceptrons (MLP), regularized linear models (Ridge and Lasso), random forests (RF), histogram-based gradient boosting (HGB), and k-nearest neighbors (KNN). Hyperparameters for each regressor were optimized using grid search with five-fold cross-validation on the training dataset, employing a variance-weighted coefficient of determination ( $R_{vw}^2$ , Eq. 10) as the selection criterion. The hyperparameter search spaces were summarized in Table 1.

$$R_{\text{pred},d}^2 = 1 - \frac{\sum_{s=1}^S (y_{s,d} - \hat{y}_{s,d})^2}{\sum_{s=1}^S (y_{s,d} - \bar{y}_d)^2} \quad (9)$$

$$R_{vw}^2 = \frac{\sum_{d=1}^D \text{Var}(y_d) \cdot R_{\text{pred},d}^2}{\sum_{d=1}^D \text{Var}(y_d)} \quad (10)$$

Table 1: Regression models and hyperparameter ranges optimized through cross-validation grid-search.

Model	Hyperparameters (default parameter or range)
MLP	Hidden layer sizes: {10, 15, 20}, activation: 'relu', learning rate: {0.01, 0.1}, max iterations: 200, early stopping with patience: 20
Ridge	Regularization strength: $\alpha \in \{0.001, 0.01, 0.1, 1.0, 10.0\}$
Lasso	Regularization strength: $\alpha \in \{0.01, 0.1, 1.0, 10.0\}$ , max iterations: 10000, tolerance: 1e-3
RF	Number of trees: {25, 50}, maximum depth: {10, 20}, maximum features: {'sqrt', 'log2'}, bootstrap=True, max samples: 0.5
HGB	Maximum iterations: 50, learning rate: {0.01, 0.1}, maximum depth: {3, 5}, max features: 0.8, early stopping with patience: 20
KNN	Number of neighbors: {10, 30, 50}, weights: {'uniform', 'distance'}

*Acronyms:* MLP – Multilayer Perceptron; RF – Random Forest; HGB – Histogram-Based Gradient Boosting; KNN – k-Nearest Neighbors.

### 2.8. Performance Assessment

We evaluated the multi-output regression models performance on a separate test dataset by computing the coefficient of determination ( $R_{\text{pred},d}^2$ ) for

each output signal  $d$  (Eq. 9), and then aggregated the results across all outputs using the variance-weighted formula (Eq. 10), where  $y_{s,d}$  and  $\hat{y}_{s,d}$  denote the true and predicted values for output  $d$  at sample  $s$ ;  $\bar{y}_d$  was the mean of the true values for output  $d$ ;  $S$  was the total number of samples; and  $D$  was the number of output signals. The term  $\text{Var}(y_d)$  represents the variance of output  $d$ , which serves as the weighting factor in the computation of  $R_{\text{vw}}^2$ .

Three complementary metrics were used to evaluate the performance of each algorithm: root mean square error (RMSE, Eq. 11), mean absolute error (MAE, Eq. 12), and Pearson's correlation coefficient ( $r$ , Eq. 13). Each metric was summarized using its variance-weighted version to account for differences in signal variability across outputs. For a given metric  $M$ , the global score  $\bar{M}$  was computed according to Eq. 14, where  $M_d$  represents the metric value for output  $d$  and  $\text{Var}(y_d)$  denotes the variance of the corresponding signal.

$$\text{RMSE}_d = \sqrt{\frac{1}{S} \sum_{s=1}^S (y_{s,d} - \hat{y}_{s,d})^2} \quad (11)$$

$$\text{MAE}_d = \frac{1}{S} \sum_{s=1}^S |y_{s,d} - \hat{y}_{s,d}| \quad (12)$$

$$r_d = \frac{\sum_{s=1}^S (y_{s,d} - \bar{y}_d) (\hat{y}_{s,d} - \bar{\hat{y}}_d)}{\sqrt{\sum_{s=1}^S (y_{s,d} - \bar{y}_d)^2} \sqrt{\sum_{s=1}^S (\hat{y}_{s,d} - \bar{\hat{y}}_d)^2}} \quad (13)$$

$$\bar{M}_{\text{vw}} = \frac{\sum_{d=1}^D \text{Var}(y_d) M_d}{\sum_{d=1}^D \text{Var}(y_d)} \quad (14)$$

### 2.9. Sensitivity Analysis of Processing and Modeling Parameters

We conducted a sensitivity analysis to quantify the impact of individual processing and modeling parameters on decoding performance. For each analysis, we systematically varied a single parameter while keeping the remaining settings fixed, allowing us to isolate its specific contribution. Across all experiments, we maintained the following control settings: a block size of  $2 \times 2$ , a step size of  $s = 1$ , a window length of 150 ms with an overlap of 50 ms, and time-windowed sequences constructed with a single-sample window ( $n_{\text{win}} = 1$ ). These settings provided a consistent baseline for evaluating the effect of each factor.

*Spatial-Domain parameters.* We assessed spatial aggregation effects by varying the block size from  $1 \times 1$  (single-channel) to  $8 \times 8$  (full-grid). We also evaluated the impact of spatial sub-sampling by varying the step size  $e$  between 1 and 6.

*Temporal-Domain parameters.* Next, we examined temporal processing parameters to analyze how signal integration and sequence structure influence decoding. We investigated the effect of temporal integration by varying the window length  $L$  from 100 to 500 ms in increments of 50 ms. During the regression modeling stage, we incorporated temporal dependencies by varying the number of consecutive samples per input sequence  $n_{\text{win}}$  between 1 and 10. We generated time-windowed sequences by applying a sliding window to the HD sEMG features and the corresponding joint angle signals, before shuffling the training data. Each window contained  $n_{\text{win}}$  consecutive samples, which we flattened and concatenated to form the feature vector  $X \in \mathbb{R}^{n_{\text{win}} \cdot n_{\text{feat}}}$  and the target vector  $y \in \mathbb{R}^{n_{\text{win}} \cdot n_{\text{out}}}$ . The sliding window was advanced by one sample to maximize overlap between consecutive sequences. By varying  $n_{\text{win}}$ , we systematically captured temporal dependencies at multiple time scales, from short-term fluctuations to longer contextual dynamics in the EMG–kinematic relationship. After generating predictions, we reconstructed the time series by sequentially concatenating the last prediction of each window, preserving the temporal structure of the original signals while enabling supervised learning with fixed-size input–output pairs.

### 2.10. Sequential Forward Block Selection Algorithm

Sequential forward selection (SFS) is a greedy search algorithm that incrementally builds an optimal feature subset by maximizing a predefined performance metric, such as classification accuracy. The procedure starts with an empty set and, at each iteration, adds the single feature that provides the greatest improvement according to the objective function [19]. Sequential forward block Selection (SFBS) extends the latter approach by selecting entire spatial blocks rather than individual features [14]. Here, each block was represented by its corresponding MLD feature set. By evaluating blocks as unified entities, SFBS exploits the spatial organization of the data and captures the joint contribution of grouped features.

We applied the SFBS algorithm to quantify the contribution of each spatial block to decoding performance. The set of candidate blocks was  $\mathcal{U} = 1, 2, \dots, B$ , and the set of selected blocks  $\mathcal{A}$  was initially empty. Each

block  $j$  represented a feature matrix  $X_j$ , and  $y$  was the target vector. At each iteration, the algorithm evaluates all remaining candidate blocks by concatenating their features with those already selected (Eq. 15), selects the block that maximizes the performance metric, and updates  $\mathcal{A}$  accordingly.

$$\mathcal{B}_i = \mathcal{A} \cup \{i\} \quad (15)$$

The algorithm trains a regression model using the features in  $\mathcal{B}_i$  and evaluates it on the test set using the  $R_{vw}^2$  metric to obtain a performance score  $s_i$ . It then selects the block  $i^*$  that maximizes  $s_i$  (Eq. 16), removes it from  $\mathcal{U}$ , and adds it to  $\mathcal{A}$ . The procedure was repeated iteratively, increasing the subset size  $n\mathcal{A} = |\mathcal{A}|$  by one at each step until all blocks were selected.

$$i^* = \arg \max_{i \in \mathcal{U}} s_i, \quad \mathcal{A} \leftarrow \mathcal{A} \cup \{i^*\}, \quad \mathcal{U} \leftarrow \mathcal{U} \setminus \{i^*\} \quad (16)$$

The algorithm recorded the performance score associated with each selected block, producing a sequence of incremental scores that reflected the contribution of each block to the overall model performance. The final output was the ordered list of selected blocks and their corresponding incremental scores. Additionally, the incremental normalized  $R_{vw}^2$  gain ( $\hat{R}_{vw}^2$ ) contributed by each channel was computed and mapped onto the electrode array to reveal potential spatial patterns of channel relevance. An  $\hat{R}_{vw}^2$  value of 1.0 indicates the highest contribution observed for a given block in a given participant. Furthermore, the centroid of the contribution maps for both the EDC and FDS electrode arrays was calculated and reported in terms of their row and column coordinates (row, column).

### 2.11. Feature Comparison

We compared the proposed MLD-BFM representation against four alternative feature sets: (1) RMS values from all channels, referred to as RMS; (2) time-domain features consisting of mean absolute value (MAV) and waveform length from all channels, referred to as MAV-WL; (3) RMS values decomposed using Non-Negative Matrix Factorization initialized with nonnegative double singular value decomposition and small random values, using the multiplicative update solver, referred to as NMF; and (4) RMS values decomposed using Principal Component Analysis, referred to as PCA.

For the decomposition-based feature sets (i.e., NMF and PCA), the optimal number of components for each participant was determined using a plateau-based strategy [20, 21]. In this method, up to 19 components were initially extracted to construct the variance-explained ( $R_{\text{var}}^2$ , Eq. 17) curve as a function of the number of components. The  $R_{\text{var}}^2$  was computed by reconstructing the original EMG RMS signals from the extracted components and comparing the reconstructed signals with the originals. The plateau was identified as the point along the  $R_{\text{var}}^2$  curve beyond which additional components yielded only marginal gains, indicating a saturation of explained variance. Linear fits were sequentially applied to portions of the  $R_{\text{var}}^2$  curve, and the mean squared error (MSE) of each fit was computed. The first point for which the MSE fell below a predefined threshold ( $10^{-6}$  in the present study) was selected as the optimal number of components  $N^*$ . This procedure objectively estimated the minimal number of components that sufficiently captured the variance of the original EMG RMS feature set, balancing dimensionality reduction and information preservation.

$$R_{\text{var}}^2 = \frac{1}{C} \sum_{c=1}^C \left[ 1 - \frac{\sum_{n=1}^N (x_{n,c} - \hat{x}_{n,c})^2}{\sum_{n=1}^N (x_{n,c} - \bar{x}_c)^2} \right] \quad (17)$$

### 2.12. Statistical Analysis

To evaluate whether the feature sets and optimization hyperparameters of the MLD-BFM yielded statistically significant differences in predictive performance, we first assessed the normality of the  $R_{\text{vw}}^2$  distributions for each group using the D'Agostino–Pearson test. Because the data systematically violated the normality assumption, we applied non-parametric tests. Three multifactorial Kruskal–Wallis tests were conducted to examine overall differences across: (i) optimization hyperparameters and regression models; (ii) feature sets and regression models; and (iii) fingers, using the best-performing combination of feature set and regression model.

Effect sizes were reported using Epsilon squared ( $\varepsilon^2$ ) [22], categorized as negligible for  $\varepsilon^2 < 1\%$ , small for  $1\% \leq \varepsilon^2 < 8\%$ , medium for  $8\% \leq \varepsilon^2 < 26\%$ , and large for  $\varepsilon^2 \geq 26\%$  [23]. *post* pairwise comparisons were conducted using Dunn's test with Bonferroni correction to adjust for multiple comparisons. Pairwise differences were visualized using a compact letter display generated with the insert–absorb algorithm and sweeping [24], in which groups sharing at least one letter are not significantly different, whereas groups with no

letters in common differ significantly. All tests adopted a significance level of  $p < 0.05$ . All metrics and descriptive statistics were reported as mean  $\pm$  95% confidence interval.

### 3. Results

#### 3.1. Effect of Block Size

Regressor performance varied systematically with block size (Fig. 3). The Kruskal–Wallis test revealed a large and significant main effect of block size ( $p < 0.001, \varepsilon^2 = 48.57\%$ ), a medium effect of the regression model ( $p < 0.001, \varepsilon^2 = 17.50\%$ ), and a large effect of their interaction ( $p < 0.001, \varepsilon^2 = 70.50\%$ ) on predictive performance. Post-hoc Dunn tests confirmed that these differences were statistically significant for all regressors. For MLP, Ridge, and Lasso, block sizes 2–4 outperformed larger blocks (7–8). Ridge and Lasso also showed significant contrasts between block sizes 2–3 and intermediate sizes (6–7). Random Forest exhibited fewer but still significant differences, mainly between block size 2 and larger sizes (6–8;  $p < 0.05$ ). HGB displayed a similar pattern, with significant differences between block sizes 1–4 and 7–8. KNN also showed significant pairwise differences between smaller (2–3) and larger (6–8) block sizes.

Across all regressors, the highest  $R_{vw}^2$  scores occurred at block size 2, with performance peaking for MLP ( $86.68 \pm 0.33$ ) and remaining high for HGB ( $82.09 \pm 0.38$ ), KNN ( $79.60 \pm 0.56$ ), Ridge ( $79.55 \pm 0.94$ ), and Lasso ( $78.10 \pm 0.42$ ). Accuracy declined monotonically as block size increased, reaching substantially lower values at block size 8 across all models. Smaller blocks, particularly block size 2, provided the most effective feature representation, whereas larger blocks consistently degraded predictive performance.

#### 3.2. Effect of Block Step

Algorithm performance exhibited a clear dependence on block step size (Fig. 4). The Kruskal–Wallis test revealed a medium but significant main effect of block step size ( $p < 0.001, \varepsilon^2 = 22.28\%$ ), a large effect of the regression model ( $p < 0.001, \varepsilon^2 = 28.61\%$ ), and a large effect of their interaction ( $p < 0.001, \varepsilon^2 = 55.83\%$ ) on predictive performance. Across all regressors, smaller block steps generally yielded higher  $R_{vw}^2$  scores. The highest  $R_{vw}^2$  values were observed for MLP at block step 1, although no statistically significant differences were detected across block steps for this estimator.

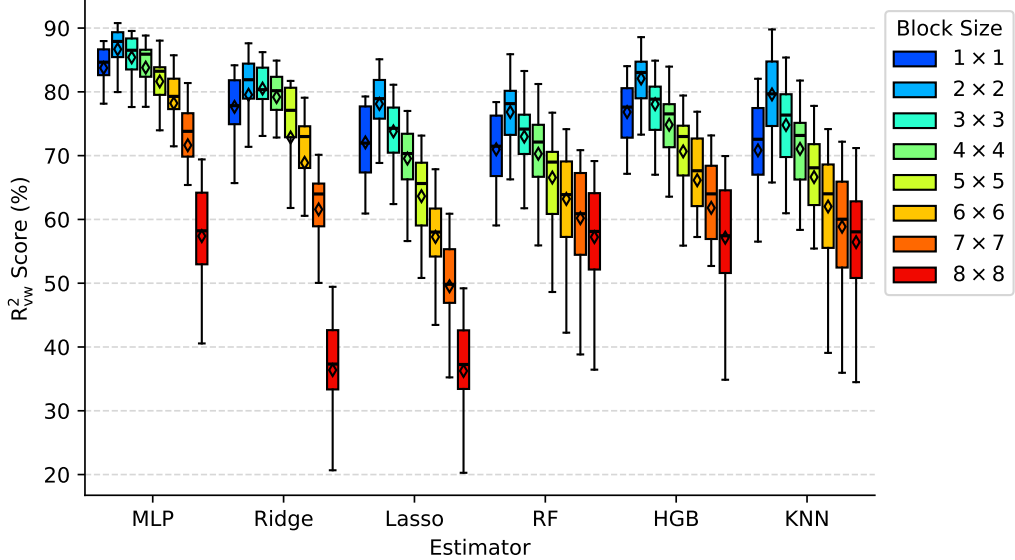


Figure 3: Distribution of  $R^2_{vw}$  scores across participants, evaluating the performance of the MLD-BFM feature extraction method ( $N = 21$ ). Results are presented for various block sizes and six regression models: Multilayer Perceptron (MLP), Ridge, Lasso, Random Forest (RF), Histogram Gradient Boost (HGB), and k-Nearest Neighbors (KNN).

*Post hoc* pairwise comparisons using Dunn’s test with the Bonferroni correction confirmed that these differences were statistically significant for the Ridge and Lasso models, but not for the MLP, RF, HGB, or KNN models. For Ridge, smaller block steps (1 and 2) significantly outperformed larger ones (4, 5, and 6) ( $p < 0.001$ ), and block step 2 also showed significant advantages over block steps 5 and 6 ( $p < 0.01$ ). Similarly, for Lasso, block steps 1 and 2 achieved significantly higher performance than block steps 4 and 5 ( $p < 0.05$ ). These results indicate that block step size critically affects decoding performance for linear models, with small steps providing more informative feature representations, while larger steps systematically degrade predictive accuracy.

### 3.3. Effects of Feature Window

Model performance also depended systematically on the temporal window length used to compute block features (Fig. 5). The Kruskal–Wallis test revealed a large and significant main effect of window size ( $p < 0.001$ ,  $\varepsilon^2 = 39.51\%$ ), a small effect of the regression model ( $p < 0.001$ ,  $\varepsilon^2 = 7.49\%$ ), and

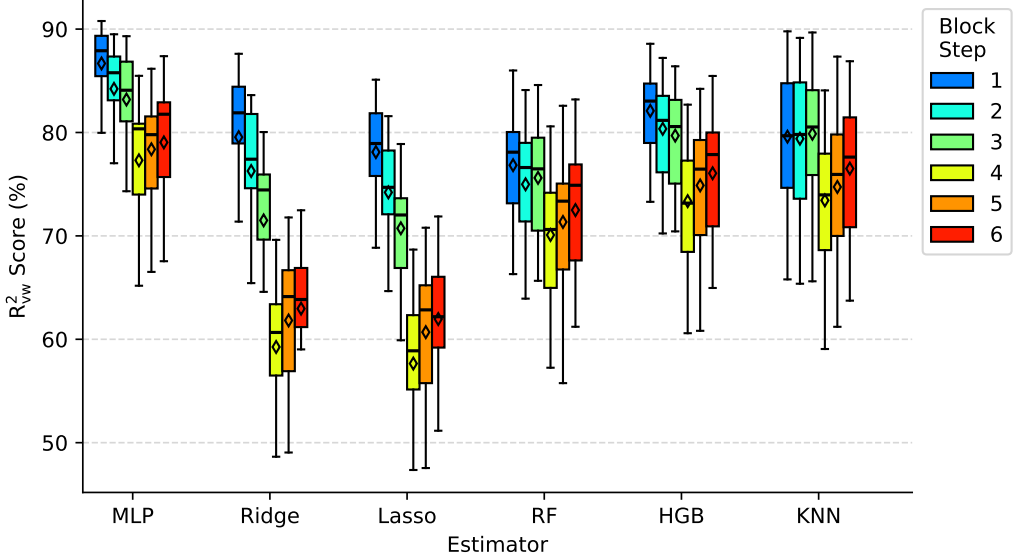


Figure 4: Distribution of  $R^2_{vw}$  scores across participants, evaluating the performance of the MLD-BFM feature extraction method ( $N = 21$ ). Results are presented for various block steps and regression models, including Multilayer Perceptron (MLP), Ridge, Lasso, Random Forest (RF), Histogram Gradient Boost (HGB), and k-Nearest Neighbors (KNN).

a large effect of their interaction ( $p < 0.001$ ,  $\varepsilon^2 = 52.28\%$ ) on predictive performance.

Post-hoc Dunn's tests confirmed significant pairwise differences for most regressors. MLP and Ridge showed markedly higher performance for intermediate windows (100–150 ms) compared to larger ones (400–500 ms). Ridge also differed from mid-range windows (250–300 ms). Lasso, HGB, and KNN exhibited similar patterns, with intermediate windows outperforming larger ones. In contrast, RF showed no significant differences, indicating a more constant performance profile.

Across all regressors, the highest  $R^2_{vw}$  scores occurred at a window size of 150 s, with performance peaking for MLP ( $86.68 \pm 0.33$ ) and remaining high for HGB ( $82.09 \pm 0.38$ ), KNN ( $79.60 \pm 0.56$ ), Ridge ( $79.55 \pm 0.94$ ), and Lasso ( $78.10 \pm 0.42$ ). As the window length increased beyond 150 ms, accuracy declined progressively, reaching its lowest values at 500 ms across all models. Intermediate windows, therefore, offered the best balance between temporal resolution and predictive information, whereas larger windows consistently degraded predictive performance.

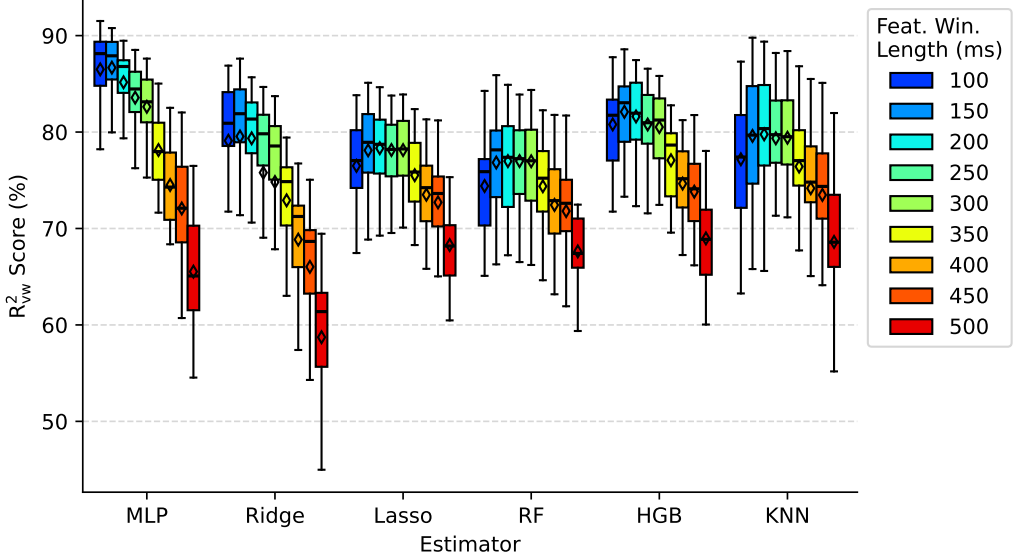


Figure 5: Distribution of  $R^2_{vw}$  scores across participants, evaluating the performance of the MLD-BFM feature extraction method ( $N = 21$ ). Results are presented for various feature window lengths and regression models, including Multilayer Perceptron (MLP), Ridge, Lasso, Random Forest (RF), Histogram Gradient Boost (HGB), and k-Nearest Neighbors (KNN).

### 3.4. Effects of Time-Windowed Sequence Construction

The number of training samples alone did not significantly affect model performance (Fig. 6). The Kruskal–Wallis test revealed no main effect of sequence size ( $p = 0.865$ ,  $\varepsilon^2 = 0.37\%$ ), but detected medium effects of the regressor ( $p < 0.001$ ,  $\varepsilon^2 = 20.48\%$ ) and their interaction with sample size ( $p < 0.001$ ,  $\varepsilon^2 = 26.44\%$ ).

Despite the absence of a main effect of training sequence size, clear performance differences were observed across regression models. Overall, MLP consistently achieved the highest  $R^2_{vw}$  values, with reference performance of  $86.68 \pm 0.33$ , significantly outperforming RF, KNN, and Lasso across multiple sequence sizes. Ridge, Lasso, and HGB exhibited intermediate performance levels, with representative values of  $82.60 \pm 0.41$ ,  $83.51 \pm 0.37$ , and  $83.88 \pm 0.34$ , respectively. In contrast, RF yielded lower predictive accuracy ( $77.01 \pm 0.46$ ), while KNN showed similarly reduced performance, with reference values near  $79.52 \pm 0.81$ . These results indicate that model choice played a substantially larger role than the number of training samples in determining decoding

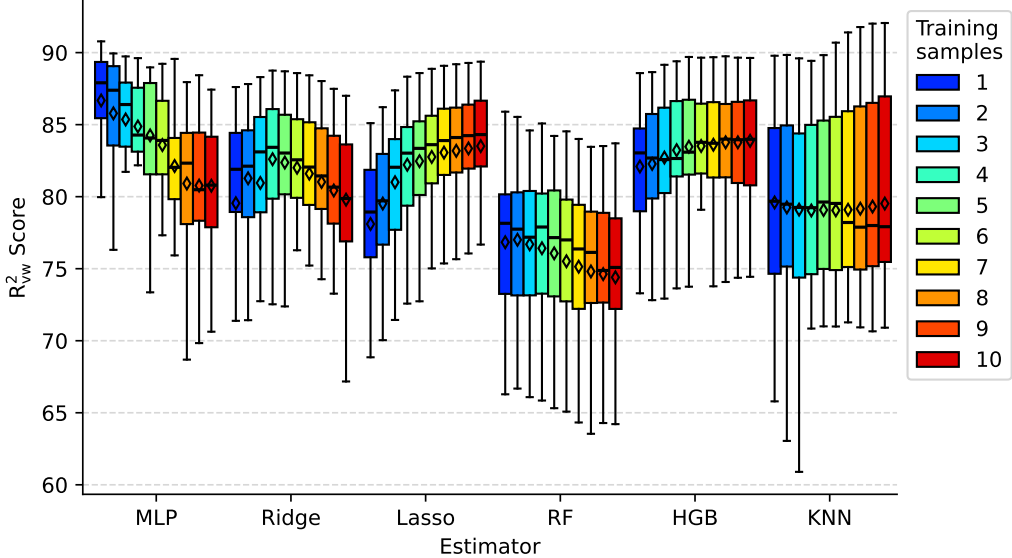


Figure 6: Distribution of  $R^2_{vw}$  scores across participants, evaluating the performance of the MLD-BFM feature extraction method ( $N = 21$ ). Results are presented for various numbers of training samples and regression models, including Multilayer Perceptron (MLP), Ridge, Lasso, Random Forest (RF), Histogram Gradient Boost (HGB), and k-Nearest Neighbors (KNN).

performance.

### 3.5. Sequential Forward Block Selection

The Sequential Forward Block Selection (SFBS) strategy applied to the MLD-BFM feature was evaluated using the Ridge regression model due to its closed-form solution and low computational complexity, which makes it well suited for iterative feature selection procedures. Across all block sizes,  $R^2_{vw}$  increased rapidly with the addition of the first blocks, followed by a plateau and a slight decline (Fig. 7). For block size 2,  $R^2_{vw}$  rose from  $34.86 \pm 3.47\%$  with the first block to a maximum of  $82.74 \pm 1.64\%$  at position 64. Block sizes 3 through 7 exhibited similar rapid initial gains, with initial  $R^2_{vw}$  values ranging from  $27.23 \pm 3.38\%$  to  $32.59 \pm 3.53\%$ . Overall, smaller block sizes reached higher peak  $R^2_{vw}$  values but required more sequential positions to do so, whereas larger block sizes peaked earlier but at lower  $R^2_{vw}$  levels. The slight decline observed after the maximum likely reflects overfitting or redundancy introduced by including additional, less informative, overlapping

blocks.

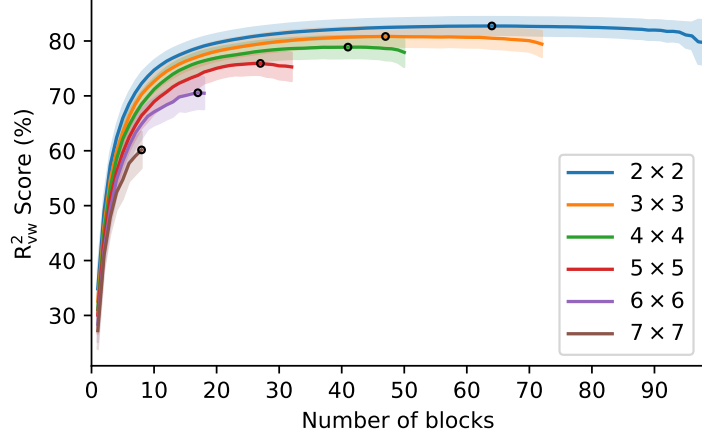


Figure 7: Performance of the Sequential Forward Block Selection (SFBS) as a function of the number of blocks and block size. The solid line represents the mean value of the population, circular markers indicate the maximum performance value for each curve, and the shaded area represents the 95% confidence interval.

The contribution of individual electrodes to performance, measured by the added  $\hat{R}_{vw}^2$  across block sizes ranging from  $2 \times 2$  to  $5 \times 5$ , is shown in Fig. 8. Analysis of the contribution maps revealed consistent spatial patterns across block sizes. For the  $2 \times 2$  and  $3 \times 3$  blocks, the highest contributions were clustered in the top-right portion of both electrode arrays. This localized pattern suggests that the linear descriptors contain highly relevant information concentrated in a specific region.

The centroid analysis revealed systematic spatial shifts as block size increased from  $2 \times 2$  to  $5 \times 5$  for both the EDC and FDS arrays. For the EDC array, the centroid started at  $(4.34 \pm 0.56, 4.97 \pm 0.53)$  with block size  $2 \times 2$  and progressively shifted toward the center, reaching  $(4.37 \pm 0.31, 4.35 \pm 0.30)$  with block size  $5 \times 5$ . This displacement was characterized by minimal variation along the column axis, while a consistent shift along the row axis toward more distal regions was observed, with the trajectory progressing from the upper-right corner toward the center of the electrode grid. For the FDS array, the shift was more pronounced: the centroid moved from  $(6.09 \pm 0.44, 5.26 \pm 0.43)$  for block size  $2 \times 2$  to  $(5.21 \pm 0.23, 4.99 \pm 0.27)$  for block size  $5 \times 5$ . This change reflects both a distal and medial shift of the added  $\hat{R}_{vw}^2$ .

To illustrate these spatial patterns in greater detail, Fig. 9 shows the

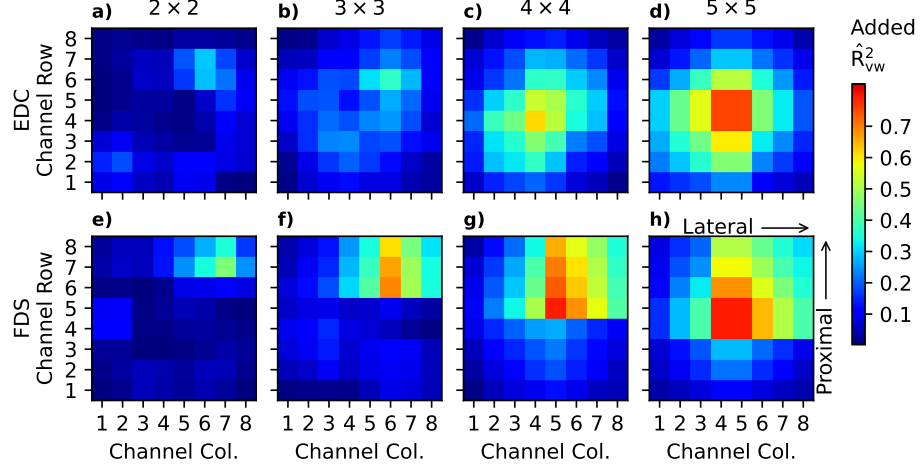


Figure 8: Heatmaps showing the average contribution of each channel in the electrode array, placed over the Extensor Digitorum Communis (EDC) and Flexor Digitorum Superficialis (FDS), to the overall performance across participants. Panels a–d) correspond to the EDC with block sizes from  $2 \times 2$  to  $5 \times 5$ , while panels e–h) correspond to the FDS with the same block sizes.

spatial arrangement of the first seven feature blocks selected by the SFBS method using  $2 \times 2$  blocks within the EDC and FDS arrays. The corresponding block feature set signals (shown using the same color code) and the regression model estimates across all tasks and for each individual finger are presented in Fig. 10.

### 3.6. Regression Performance on Different Feature Sets

To evaluate the regression performance of different feature sets, we first determined the optimal number of components for PCA- and NMF-based dimensionality reduction methods. Both methods exhibited a rapid initial increase in  $R^2_{\text{var}}$  as components were added, followed by a clear saturation trend (Fig. 11). The plateau values reached  $98.57 \pm 0.31\%$  for PCA and  $98.05 \pm 0.34\%$  for NMF, with  $7.03 \pm 0.46\%$  and  $7.41 \pm 0.52\%$  components, respectively. Although the optimal number of components was determined individually for each participant, these values reflect the overall trend of the participant sample as a whole. Taken together, the results show that for both techniques, approximately seven components were sufficient to capture nearly all the variance of the RMS values of HD sEMG signals, with additional components providing only marginal gains in explained variance.

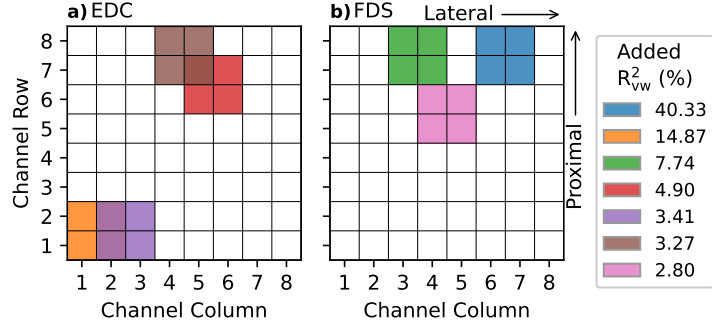


Figure 9: Representative example of the relative positions of the seven most relevant blocks for Ridge regression algorithm within the electrode arrays. (a) Array over the Extensor Digitorum Communis (EDC) muscle. (b) Array over the Flexor Digitorum Superficialis (FDS) muscle.

The Kruskal–Wallis test revealed a significant and large effect of the feature set ( $p < 0.001$ ,  $\epsilon^2 = 43.96\%$ ), a medium effect of the estimator model ( $p < 0.001$ ,  $\epsilon^2 = 15.73\%$ ), and a large effect of their interaction ( $p < 0.001$ ,  $\epsilon^2 = 66.46\%$ ) on  $R^2_{vw}$ . *Post hoc* Dunn’s tests indicated that NMF differed significantly from MLD-BFM across all regressor models. PCA also differed significantly from MLD-BFM for most regressors, except for KNN and RF, for which no significant differences were observed. Furthermore, PCA and NMF showed significant differences from MAV-WL and RMS features when combined with MLP, Ridge, and Lasso. The results are illustrated in Fig. 12, which presents each feature–regressor combination along with the corresponding *post hoc* comparisons between feature sets for each regression model.

MLD-BFM achieved the highest  $R^2_{vw}$  values across all models, with MLP reaching the best overall performance ( $86.68 \pm 0.33\%$ ) and HGB following closely ( $82.09 \pm 0.38\%$ ). KNN and Ridge yielded intermediate values ( $79.60 \pm 0.56\%$  and  $79.55 \pm 0.94\%$ , respectively), whereas Lasso and RF produced the lowest scores ( $78.10 \pm 0.42\%$  and  $76.84 \pm 0.48\%$ ). Despite achieving the highest values, MLD-BFM did not differ significantly from MAV-WL and RMS features for most models. MAV-WL and RMS also showed strong predictive performance, with MLP reaching  $84.99 \pm 0.38\%$  and  $81.46 \pm 0.79\%$ , respectively, and HGB yielding slightly lower values ( $77.08 \pm 0.52\%$  and  $74.06 \pm 0.57\%$ ). PCA and NMF generally underperformed, with their best results obtained with KNN ( $72.41 \pm 0.89\%$  for PCA and  $63.43 \pm 1.44\%$  for

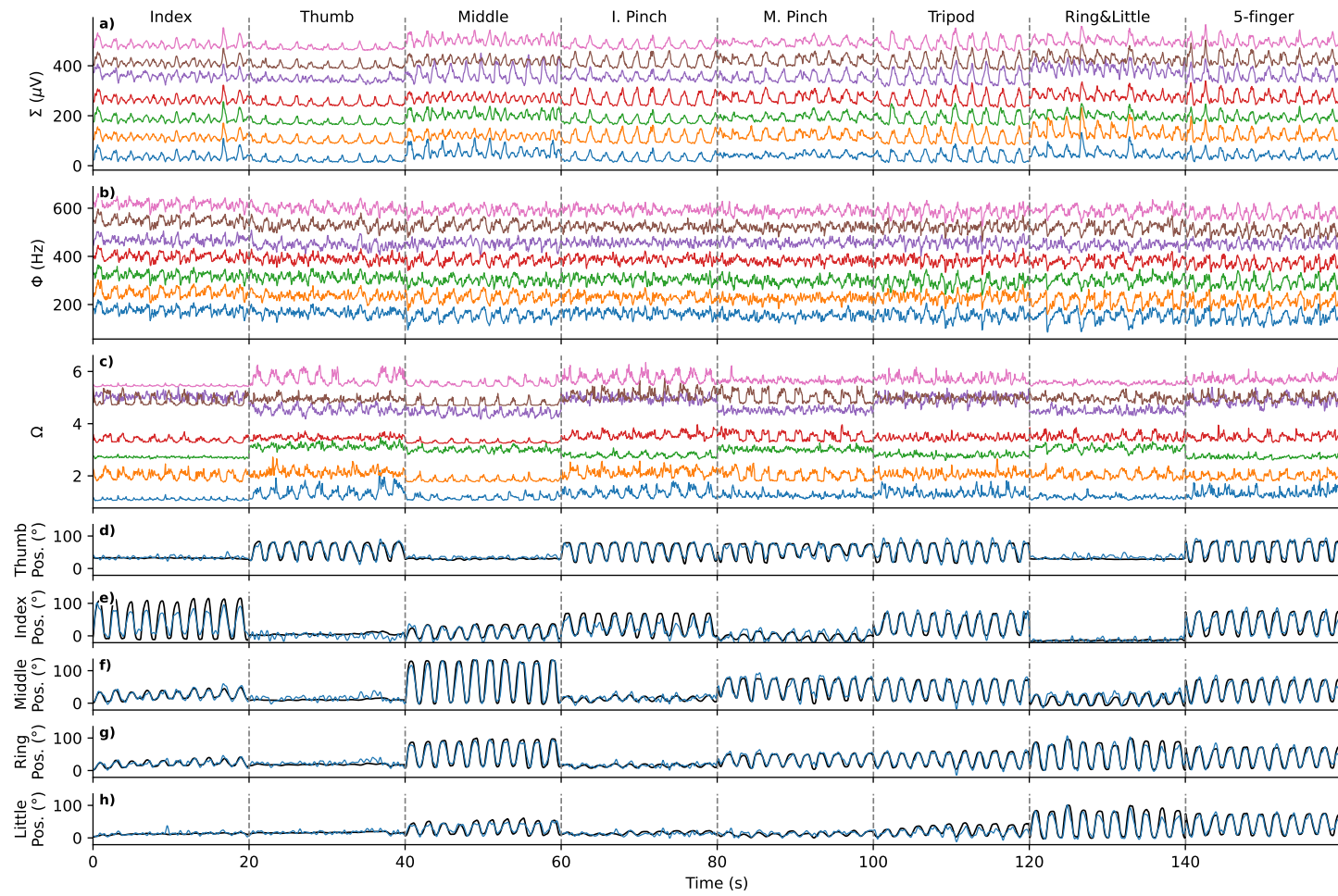


Figure 10: Representative example of the test data, highlighting the feature set and the agreement between computed and predicted finger angular positions. The analysis was performed using the Ridge regression algorithm with a block size of  $2 \times 2$ , a step of 1, a window duration of 150 ms, and with each sliding window treated as an individual testing sample. Subplots (a)–(c) show the feature set for the seven most relevant blocks, corresponding to effective field strength ( $\Sigma$ ), field-strength variation rate ( $\Phi$ ), and spatial complexity ( $\Omega$ ). Subplots (d)–(h) compare the computed and predicted angular positions for the Thumb, Index, Middle, Ring, and Little fingers.

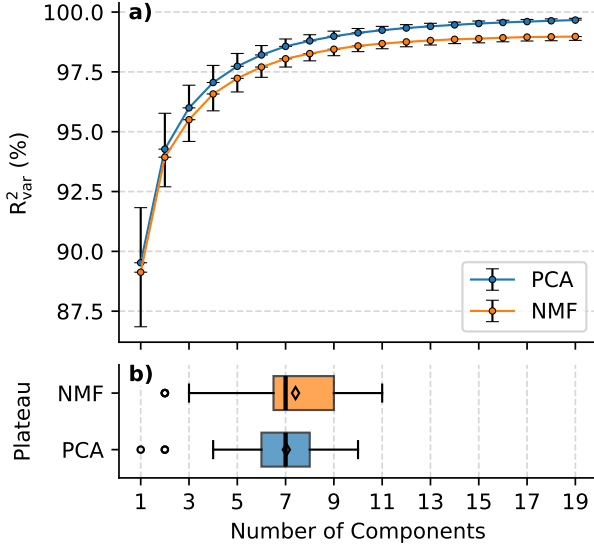


Figure 11: (a) Relationship between the explained variance of the reconstructed RMS values of HD sEMG signals and the number of components for the Non-negative Matrix Factorization (NMF) and Principal Component Analysis (PCA). Markers indicate mean values, and error bars represent the 95 % confidence interval ( $N = 21$ ). (b) Distribution of the number of components determined by the plateau method for NMF and PCA. Diamonds denote mean values, boxes represent the interquartile range, and whiskers indicate minimum and maximum values (excluding outliers - white circles).

NMF). Table 2 summarizes the best-performing regressor for each feature set.

The results for individual fingers across feature sets and regression models are presented in Fig. 13. The Kruskal-Wallis test revealed a large effect of the feature-regressor factor ( $p < 0.001$ ,  $\varepsilon^2 = 42.88\%$ ), a medium effect of the finger factor ( $p < 0.001$ ,  $\varepsilon^2 = 11.24\%$ ), and a large effect of their interaction ( $p < 0.001$ ,  $\varepsilon^2 = 54.87\%$ ). The results indicate that most of the variance in decoding accuracy stems from the choice of feature set and regression model, that performance varies to a moderate extent across fingers, and that the interaction between feature-regressor combinations and specific accounts for a large proportion of the variance in performance.

Dunn's *post hoc* tests showed that MLD-BFM with MLP consistently outperformed NMF with KNN across all fingers ( $p < 0.01$ ) and differed significantly from PCA with KNN for most fingers, except for the thumb. No significant differences emerged between MLD-BFM (MLP), MAV-WL (MLP)

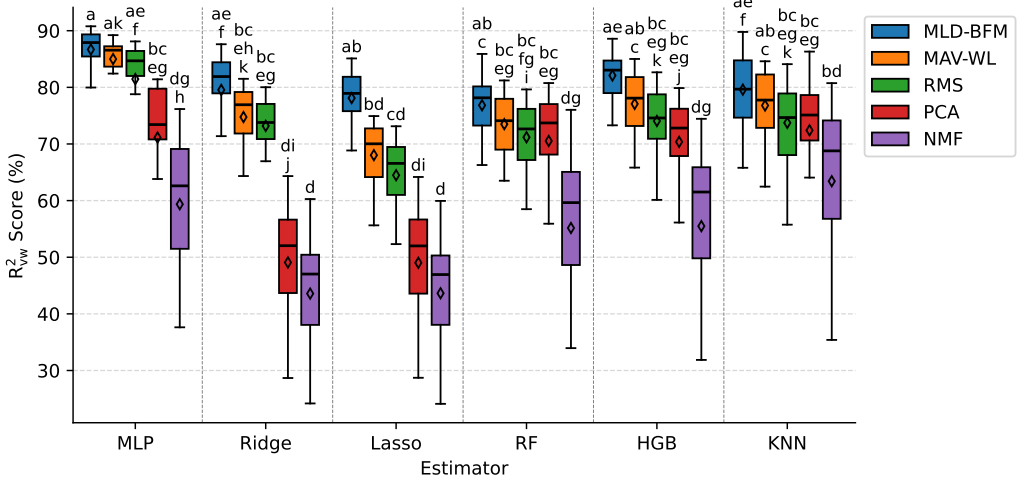


Figure 12: Distribution of the  $R^2_{vw}$  score ( $N = 21$ ) as a function of the feature set (MLD-BFM, MAV-WL, RMS, PCA, and NMF) and the regression model (Multilayer Perceptron — MLP, Ridge, Lasso, Random Forest — RF, Histogram Gradient Boosting — HGB, and k-Nearest Neighbors — KNN). Diamonds denote mean values, boxes represent the interquartile range, and whiskers indicate minimum and maximum values (excluding outliers). *Post hoc* comparisons (Dunn’s test with Bonferroni correction,  $p < 0.05$ ) were summarized using a compact letter display to ensure clarity. Groups that do not share a letter are significantly different.

or RMS (MLP), indicating statistically comparable performance among these three approaches within each finger.

MLD-BFM with MLP yielded the highest  $R^2_{pred}$  values for all fingers, ranging from  $81.34 \pm 0.53\%$  for the thumb to  $89.12 \pm 0.21\%$  for the middle finger. MAV-WL (MLP) achieved slightly lower results ( $78.69 \pm 0.72\%$  for the thumb and  $87.45 \pm 0.30\%$  for the middle finger), confirming that simple time-domain features retain substantial predictive power. RMS features followed a similar pattern but showed a more pronounced drop for the thumb ( $74.69 \pm 1.21\%$ ), while still reaching  $83.74 \pm 1.03\%$  for the middle finger. In contrast, dimensionality reduction approaches underperformed: PCA with KNN achieved moderate accuracy for the middle ( $78.84 \pm 0.67\%$ ) and ring ( $76.39 \pm 0.90\%$ ) fingers but dropped to approximately 66% for the thumb and index. NMF with KNN consistently yielded the lowest performance, with values as low as  $55.58 \pm 1.85\%$  for the index finger.

Table 2: Results obtained for each feature set using its best-performing regressor model.

Feature	Estimator	$R^2_{vw}$ Score (%)	RMSE (°)	MAE (°)	Pearson $r$
MLD-BFM	MLP	$86.68 \pm 0.34$	$10.98 \pm 0.17$	$7.99 \pm 0.12$	$0.93 \pm 0.00$
MAV-WL	MLP	$84.99 \pm 0.39$	$11.72 \pm 0.19$	$8.63 \pm 0.14$	$0.92 \pm 0.00$
RMS	MLP	$81.46 \pm 0.81$	$12.86 \pm 0.26$	$9.32 \pm 0.18$	$0.90 \pm 0.00$
PCA	KNN	$72.41 \pm 0.92$	$15.76 \pm 0.30$	$11.01 \pm 0.25$	$0.84 \pm 0.01$
NMF	KNN	$63.43 \pm 1.47$	$18.10 \pm 0.40$	$12.62 \pm 0.31$	$0.79 \pm 0.01$

*Acronyms:* MLD-BFM – Multichannel Linear Descriptors-based Block Field Method; MAV-WL – Mean Absolut Value and Waveform Length; RMS – Root Mean Square; PCA – Principal Component Analysis; NMF – Non-negative Matrix Factorization; MLP – Multilayer Perceptron; KNN – k-Nearest Neighbors;  $R^2_{vw}$  – Variance-weighted coefficient of determination; RMSE – Root Mean Square Error; MAE – Mean Absolute Error.

## 4. Discussion

The present study aimed to systematically evaluate the MLD-BFM for the simultaneous and proportional decoding of five DoFs of finger joint movements, leveraging the rich spatial information provided by HD sEMG. The findings indicate that MLD-BFM consistently achieved the highest performance values across all tested regression models, with the MLP model reaching the overall best performance. While conventional time-domain features also demonstrated strong predictive capabilities and were statistically comparable to MLD-BFM for most models, dimensionality reduction techniques such as PCA and NMF yielded substantially lower accuracy comparatively. Overall, the results highlight the importance of preserving the spatial richness of HD sEMG for SPC, providing evidence that spatially structured features enhance decoding accuracy and can contribute to the development of more natural and responsive real-time myoelectric interfaces.

### 4.1. Influence of Spatial and Temporal Parameters on MLD-BFM Decoding Performance

The parameter analysis of MLD-BFM demonstrated that block size constitutes a critical determinant of prediction accuracy, with the  $2 \times 2$  configuration yielding the highest performance. The result is consistent with previous findings obtained using classification-based algorithms [14]. Importantly, the present study extends the observation to continuous multi-DoF regression, providing early evidence of the suitability of MLD-BFM features for regression models. This configuration likely achieves an optimal trade-off between

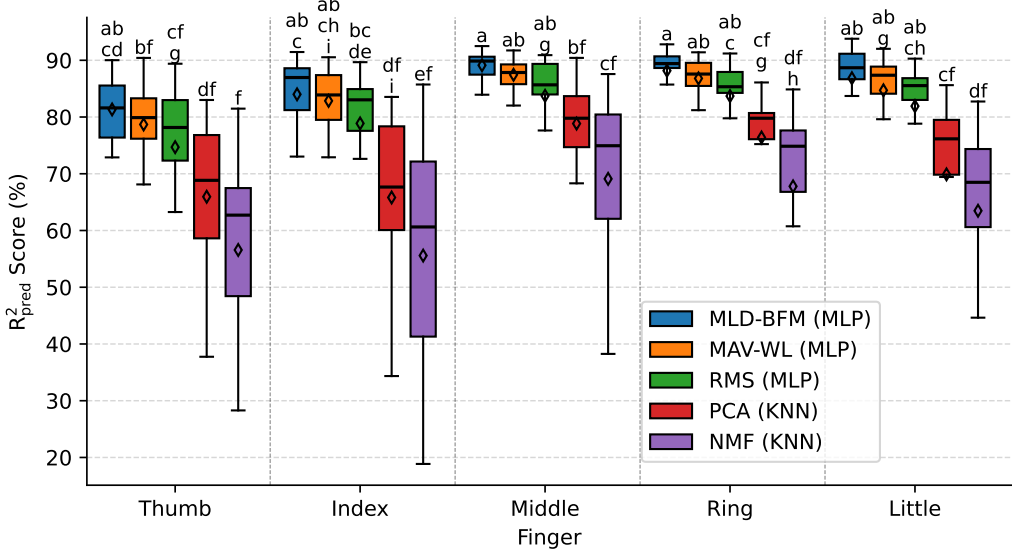


Figure 13: Distribution of the  $R^2_{\text{pred}}$  score for predicting the angular position of each finger (thumb, index, middle, ring, and little) using the best-performing model for each feature set. Diamonds denote mean values, boxes represent the interquartile range, and whiskers indicate minimum and maximum values (excluding outliers). *Post hoc* comparisons (Dunn’s test with Bonferroni correction,  $p < 0.05$ ) were summarized using a compact letter display to ensure clarity. Groups that do not share a letter are significantly different.

capturing local spatial dependencies and preserving signal complexity across channels, thereby maximizing feature expressiveness, whereas larger blocks may attenuate descriptor discriminability.

While previous studies employing classification models reported improved performance with increasing temporal window lengths [14], our results indicate an optimal window duration of approximately 150 ms. This discrepancy likely reflects differences in experimental design and objectives. In the study reported in [14], participants were instructed to perform discrete movements held for 4 s, focusing on the classification of static contractions, whereas our study involves continuous regression of dynamic sinusoidal movements.

The temporal sensitivity analysis confirmed that a 150 ms window represents the optimal parameter, yielding the highest  $R^2_{\text{vw}}$  scores across all tested regressors. This window provides an effective trade-off by capturing sufficient signal dynamics while minimizing redundancy. The optimality of the 150 ms window may be directly related to the 0.5 Hz frequency of the sinu-

soidal tasks used in this study, which provides adequate temporal resolution to capture meaningful signal fluctuations.

However, the literature highlights movement speed as a critical factor influencing algorithm performance, as fast and forceful movements generate large, distinctive EMG patterns, whereas slow movements produce subtler and noisier variations in myoelectric signals [25]. Indeed, previous studies have demonstrated a robust correlation between increased movement speed and the corresponding rise in myoelectric activity [26]. Given that most decoders are trained on homogeneous single-speed datasets, and that limited variability in training speeds can impair generalization and degrade decoder performance, future studies should investigate whether training on heterogeneous tasks comprising both slow and fast movements alters the optimal temporal window duration.

The findings indicated that smaller block steps consistently outperformed larger ones. This dependency was particularly critical for linear regression models (Ridge and Lasso). The block step determines the density and distribution of the blocks, and smaller steps maximize overlap, preserving continuity and spatial interactions between neighboring regions. As a result, they provide more informative feature representations and finer spatial resolution. Conversely, increasing the block step can be leveraged to reduce computational complexity and accelerate model processing, creating a relevant trade-off between accuracy and computational efficiency—especially in real-time applications with hardware constraints.

In the context of the SFBS technique, as the block size increased, the centroid of the added  $\hat{R}_{vw}^2$  progressively converged toward the center of both electrode grids. This trend reflects the greater spatial overlap of larger blocks with central regions and their correspondingly higher contribution to algorithm performance. Although systematic medial and distal shifts in the centroid were observed with increasing block size, the spatial locations of the most informative regions remained largely consistent within each electrode grid, particularly in the proximal-lateral areas of both the EDC and FDS grids. These findings suggest that the underlying activation patterns were preserved across block sizes and participants, and that the regions contributing most strongly to decoding performance are robust to variations in block size.

#### *4.2. Influence of Feature Extraction and Regression Methods on Decoding Performance*

The feature extraction method strongly influenced the performance of the regression models. MLD-BFM achieved the highest average performance ( $R_{vw}^2$ ) across all tested regressors, although its advantage over conventional time-domain features was not statistically significant, so that these classical amplitude-related features may remain viable alternatives when computational efficiency is a priority. Among the evaluated models, the MLP performed best when combined with MLD-BFM, likely due to its ability to efficiently capture complex nonlinear relationships. This result aligns with the widespread use of MLP as a nonlinear regressor in myoelectric control research [27, 5, 28, 6, 29]. However, this benefit comes at the expense of substantially longer training (see Supplementary Table S1) times compared to linear models such as Ridge and Lasso [6].

In contrast, the dimensionality reduction techniques explored here – principal component analysis (PCA) and non-negative matrix factorization (NMF) – consistently produced lower accuracy. This outcome supports previous findings [5], suggesting that reducing the spatial dimensionality of HD sEMG signals can impair continuous decoding performance. Interestingly, instance-based regressors like KNN partially mitigated the information loss in PCA and NMF, suggesting that local neighborhood-based methods can compensate to some extent for reduced feature sets [30].

#### *4.3. Influence of Finger on Prediction Performance*

The finger-specific analysis revealed additional insights. The middle, ring, and little fingers consistently yielded the highest predictive accuracy across feature sets and regressors, whereas the thumb exhibited the lowest predictive accuracy. A comparable pattern emerged in studies employing convolutional neural network-based models (TF2AngleNet), where the ring and little fingers achieved the best performance and thumb extension the poorest [31]. The reduced accuracy was attributed to data imbalance, with thumb movements underrepresented. In contrast, the present work included five thumb-related tasks out of eight, providing a broader representation. A similar trend was observed in a study using biomechanical models (OpenSim) driven by EMG signals, in which the thumb showed the lowest correlation with kinematic data, whereas the middle finger exhibited the highest [32].

A plausible explanation for these findings involves both anatomical and physiological factors. Electrodes are typically positioned closer to the mus-

cle groups that predominantly control the middle and ring fingers, resulting in signals with a higher signal-to-noise ratio and greater redundancy across channels. In contrast, thumb movements rely on more distributed and anatomically complex muscle activations, some of which may fall outside the optimal detection range of the electrode array, leading to reduced predictive accuracy [32]. Additionally, previous work demonstrated that the middle finger exhibits a more localized and concentrated muscle activation compared to other fingers, with its activation centroid remaining relatively stable across different forearm rotation angles [33]. This spatial consistency likely contributes to the robustness of EMG-based prediction methods for this finger. Conversely, thumb movements rely on anatomically complex and spatially distributed muscle activations that result from the coordinated combination of flexion, adduction, and pronation at the carpometacarpal joint. These movements are generated by four extrinsic and five intrinsic muscles of the thenar group, some of which may fall outside the optimal detection range of the electrode array, resulting in reduced predictive accuracy [34, 32].

#### *4.4. Limitations*

Despite the comprehensive evaluation conducted in the present study, some limitations should be acknowledged. First, the experiments were performed with a limited number of healthy participants, which may constrain the wider applicability of the findings to clinical populations or individuals with altered or reduced muscle activation patterns [35, 36]. Moreover, the predictive performance of the proposed approach was evaluated exclusively under controlled laboratory conditions, using sinusoidal finger movements at a fixed frequency, and performed under a single arm posture and contraction intensity. Such conditions may not fully reflect the variability and complexity of natural motor behaviors encountered in real-world scenarios [37, 38, 33, 25]. Second, sEMG signals are inherently susceptible to multiple sources of noise and variability, particularly during prolonged muscle activation. Factors such as perspiration-induced changes in skin impedance [39], muscle fatigue, and motor learning effects [40] can alter signal characteristics over time, potentially requiring periodic updates or adaptive strategies to maintain long-term robustness of the algorithms. In addition, manual electrode placement cannot fully eliminate positioning variability, and when displacement occurs, predictive performance can deteriorate substantially due to changes in recorded muscle activity that were not represented during model training [41, 42].

## Acknowledgments

We would like to express our gratitude to Valeria Avilés Carrillo and Guilherme A. G. De Villa for their assistance in data collection.

This work was supported by the Brazilian Public Ministry of Labor (contract number 002118.2019). Leonardo A. Elias is a recipient of a Research Productivity Fellowship from CNPq (National Council for Scientific and Technological Development, proc. no. 316320/2023-4). Kinematic data were collected using the multi-user equipment Vicon Motion Capture System, funded by FAPESP (The São Paulo Research Foundation, proc. no. 2020/13293-0).

## References

- [1] F. Cordella, A. L. Ciancio, R. Sacchetti, A. Davalli, A. G. Cutti, E. Guglielmelli, L. Zollo, Literature review on needs of upper limb prosthesis users, *Frontiers in Neuroscience* 10 (MAY) (2016) 1–14. doi:10.3389/fnins.2016.00209.
- [2] A. K. Einfeldt, F. Rebmann, D. Yao, C. Stukenborg-Colsmann, C. Hurschler, H. Windhagen, E. Jakubowitz, What do users and their aiding professionals want from future devices in upper limb prosthetics? A focus group study, *PLoS ONE* 18 (12 December) (2023) 1–14. doi:10.1371/journal.pone.0295516.  
URL <http://dx.doi.org/10.1371/journal.pone.0295516>
- [3] T. Song, Z. Yan, S. Guo, Y. Li, X. Li, F. Xi, Review of sEMG for Robot Control: Techniques and Applications, *Applied Sciences* 13 (17) (2023) 9546. doi:10.3390/app13179546.  
URL <https://www.mdpi.com/2076-3417/13/17/9546>
- [4] N. Jiang, C. Chen, J. He, J. Meng, L. Pan, S. Su, X. Zhu, Birobotics research for non-invasive myoelectric neural interfaces for upper-limb prosthetic control: a 10-year perspective review (apr 2023). doi:10.1093/nsr/nwad048.
- [5] S. Muceli, D. Farina, Simultaneous and proportional estimation of hand kinematics from EMG during mirrored movements at multiple degrees-of-freedom, *IEEE Transactions on Neural Systems and Rehabilitation Engineering* 20 (3) (2012) 371–378. doi:10.1109/TNSRE.2011.2178039.

- [6] J. M. Hahne, F. Bießmann, N. Jiang, H. Rehbaum, D. Farina, F. C. Meinecke, K. R. Muller, L. C. Parra, Linear and nonlinear regression techniques for simultaneous and proportional myoelectric control, *IEEE Transactions on Neural Systems and Rehabilitation Engineering* 22 (2) (2014) 269–279. doi:10.1109/TNSRE.2014.2305520.
- [7] A. Ameri, E. N. Kamavuako, E. J. Scheme, K. B. Englehart, P. A. Parker, Support vector regression for improved real-time, simultaneous myoelectric control, *IEEE Transactions on Neural Systems and Rehabilitation Engineering* 22 (6) (2014) 1198–1209. doi:10.1109/TNSRE.2014.2323576.
- [8] H. A. Dewald, P. Lukyanenko, J. M. Lambrecht, J. R. Anderson, D. J. Tyler, R. F. Kirsch, M. R. Williams, Stable, three degree-of-freedom myoelectric prosthetic control via chronic bipolar intramuscular electrodes: A case study, *Journal of NeuroEngineering and Rehabilitation* 16 (1) (2019) 1–13. doi:10.1186/s12984-019-0607-8.
- [9] M. Nowak, I. Vujaklija, A. Sturma, C. Castellini, D. Farina, Simultaneous and Proportional Real-Time Myocontrol of Up to Three Degrees of Freedom of the Wrist and Hand, *IEEE Transactions on Biomedical Engineering* 70 (2) (2023) 459–469. doi:10.1109/TBME.2022.3194104.
- [10] R. Merletti, S. Muceli, Tutorial. Surface EMG detection in space and time: Best practices, *Journal of Electromyography and Kinesiology* 49 (August) (2019) 102363. doi:10.1016/j.jelekin.2019.102363.  
URL <https://doi.org/10.1016/j.jelekin.2019.102363>
- [11] J. Wackermann, Beyond mapping: Estimating complexity of multichannel EEG recordings, *Acta Neurobiologiae Experimentalis* 56 (1) (1996) 197–208. doi:10.55782/ane-1996-1121.
- [12] J. Wackermann, Towards a quantitative characterisation of functional states of the brain: from the non-linear methodology to the global linear description, *International Journal of Psychophysiology* 34 (1) (1999) 65–80. doi:10.1016/S0167-8760(99)00038-0.
- [13] J. Wackermann, C. Allefeld, On the meaning and interpretation of global descriptors of brain electrical activity. Including a reply to X. Pei et

al., International Journal of Psychophysiology 64 (2) (2007) 199–210. doi:10.1016/j.ijpsycho.2007.02.003.

- [14] B. Peng, H. Zhang, X. Li, G. Li, A novel spatial feature extraction method based on high-density sEMG for complex hand movement recognition, Biomedical Signal Processing and Control 103 (November 2024) (2025). doi:10.1016/j.bspc.2024.107403.
- [15] C. M. Michel, T. Koenig, D. Brandeis, L. R. Gianotti, J. Wackermann, Electrical neuroimaging, Cambridge University Press, 2009. doi:10.1017/CBO9780511596889.
- [16] R. G. Molinari, V. Avilés-Carrillo, G. A. G. De Villa, L. A. Elias, A Wearable Platform for Real-Time Control of a Prosthetic Hand by High-Density EMG, medRxiv (2025) 1–11.
- [17] P. Zipp, Recommendations for the Standardization of Lead Positions in Surface Electromyography\*, European Journal of Applied Physiology and Occupational Physiology 50 (1982) 41–54.
- [18] B. Hjorth, The physical significance of time domain descriptors in EEG analysis, Electroencephalography and Clinical Neurophysiology 34 (3) (1973) 321–325. doi:10.1016/0013-4694(73)90260-5.
- [19] D. W. Aha, R. L. Bankert, A Comparative Evaluation of Sequential Feature Selection Algorithms, Springer New York, 1996, Ch. 19, p. 199–206. doi:10.1007/978-1-4612-2404-4\_19.
- [20] V. C. Cheung, A. D'Avella, M. C. Tresch, E. Bizzi, Central and sensory contributions to the activation and organization of muscle synergies during natural motor behaviors, Journal of Neuroscience 25 (27) (2005) 6419–6434. doi:10.1523/JNEUROSCI.4904-04.2005.
- [21] R. Ballarini, M. Ghislieri, M. Knaflitz, V. Agostini, An algorithm for choosing the optimal number of muscle synergies during walking, Sensors 21 (10) (2021) 1–15. doi:10.3390/s21103311.
- [22] M. Tomczak, E. Tomczak, The need to report effect size estimates revisited. An overview of some recommended measures of effect size, Trends in Sport Sciences 1 (21) (2014) 19–25.

- [23] S. Mangiafico, Summary and Analysis of Extension Program Evaluation in R, Rutgers Cooperative Extension, New Brunswick, NJ, version 1 Edition, retrieved from <https://rcompanion.org/handbook/> (2016). URL <https://rcompanion.org/handbook/>
- [24] H. P. Piepho, An algorithm for a letter-based representation of all-pairwise comparisons, *Journal of Computational and Graphical Statistics* 13 (2) (2004) 456–466. doi:10.1198/1061860043515.
- [25] T. N. Tully, G. S. Member, A. E. Nelson, J. A. George, A. H. Subjects, Training Movement Velocity Significantly Affects the Performance of Myoelectric Control, *IEEE Transactions on Neural Systems and Rehabilitation Engineering* PP (2025) 1. doi:10.1109/TNSRE.2025.3610352.
- [26] M. Porta, C. Filetti, A. Chiari, I. Leo, E. Padua, G. Briotti, G. Messina, W. Moalla, B. Ruscello, Examining the association between speed and myoelectric activity: Time-based differences and muscle group balance, *PLoS ONE* 19 (3 March) (2024) 1–12. doi:10.1371/journal.pone.0300117.  
URL <http://dx.doi.org/10.1371/journal.pone.0300117>
- [27] J. L. Nielsen, S. Holmgård, N. Jiang, K. B. Englehart, D. Farina, P. A. Parker, Simultaneous and proportional force estimation for multi-function myoelectric prostheses using mirrored bilateral training, *IEEE Transactions on Biomedical Engineering* 58 (3 PART 1) (2011) 681–688. doi:10.1109/TBME.2010.2068298.
- [28] N. Jiang, J. L. Vest-Nielsen, S. Muceli, D. Farina, EMG-based simultaneous and proportional estimation of wrist/hand kinematics in uni-lateral trans-radial amputees, *Journal of NeuroEngineering and Rehabilitation* 9 (1) (2012). doi:10.1186/1743-0003-9-42.
- [29] K. Z. Zhuang, N. Sommer, V. Mendez, S. Aryan, E. Formento, E. D’Anna, F. Artoni, F. Petrini, G. Granata, G. Cannaviello, W. Raffoul, A. Billard, S. Micera, Shared human–robot proportional control of a dexterous myoelectric prosthesis, *Nature Machine Intelligence* 1 (9) (2019) 400–411. doi:10.1038/s42256-019-0093-5.  
URL <http://dx.doi.org/10.1038/s42256-019-0093-5>

[30] M. Roughan, Y. Zhang, W. Willinger, L. Qiu, Spatio-temporal compressive sensing and internet traffic matrices (Extended Version), *IEEE/ACM Transactions on Networking* 20 (3) (2012) 662–676. doi:10.1109/TNET.2011.2169424.

[31] H. Jiang, Y. Yamanoi, P. Chen, X. Wang, S. Chen, X. Yong, G. Li, H. Yokoi, X. Jing, TF2AngleNet: Continuous finger joint angle estimation based on multidimensional time–frequency features of sEMG signals, *Biomedical Signal Processing and Control* 107 (October 2024) (2025) 107833. doi:10.1016/j.bspc.2025.107833.  
URL <https://doi.org/10.1016/j.bspc.2025.107833>

[32] D. Blana, A. J. Van Den Bogert, W. M. Murray, A. Ganguly, A. Krasoulis, K. Nazarpour, E. K. Chadwick, Model-Based Control of Individual Finger Movements for Prosthetic Hand Function, *IEEE Transactions on Neural Systems and Rehabilitation Engineering* 28 (3) (2020) 612–620. doi:10.1109/TNSRE.2020.2967901.

[33] N. Rubin, Y. Zheng, H. Huang, X. Hu, Finger Force Estimation using Motor Unit Discharges Across Forearm Postures, *IEEE Trans Biomed Eng* 9294 (c) (2022) 1–9. doi:10.1109/TBME.2022.3153448.

[34] V. K. Nanayakkara, G. Cotugno, N. Vitzilaios, D. Venetsanos, T. Nanayakkara, M. N. Sahinkaya, The Role of Morphology of the Thumb in Anthropomorphic Grasping: A Review, *Frontiers in Mechanical Engineering* 3 (June) (2017). doi:10.3389/fmech.2017.00005.

[35] H. Daley, K. Englehart, L. Hargrove, U. Kuruganti, High density electromyography data of normally limbed and transradial amputee subjects for multifunction prosthetic control, *Journal of Electromyography and Kinesiology* 22 (3) (2012) 478–484. doi:10.1016/j.jelekin.2011.12.012.  
URL <http://dx.doi.org/10.1016/j.jelekin.2011.12.012>

[36] M. B. Kristoffersen, A. W. Franzke, C. K. Van Der Sluis, R. M. Bongers, A. Murgia, Should Hands Be Restricted When Measuring Able-Bodied Participants to Evaluate Machine Learning Controlled Prosthetic Hands?, *IEEE Transactions on Neural Systems and Rehabilitation Engineering* 28 (9) (2020) 1977–1983. doi:10.1109/TNSRE.2020.3007803.

- [37] I. Vujaklija, A. D. Roche, T. Hasenoehrl, A. Sturma, S. Amsuess, D. Farina, O. C. Aszmann, Translating research on myoelectric control into clinics—are the performance assessment methods adequate?, *Frontiers in Neurorobotics* 11 (FEB) (2017) 1–7. doi:10.3389/fnbot.2017.00007.
- [38] E. Campbell, A. Phinyomark, E. Scheme, Current trends and confounding factors in myoelectric control: Limb position and contraction intensity, *Sensors (Switzerland)* 20 (6) (2020) 1–44. doi:10.3390/s20061613.
- [39] M. Abdoli-Eramaki, C. Damecour, J. Christenson, J. Stevenson, The effect of perspiration on the sEMG amplitude and power spectrum, *Journal of Electromyography and Kinesiology* 22 (6) (2012) 908–913. doi:10.1016/j.jelekin.2012.04.009.  
URL <http://dx.doi.org/10.1016/j.jelekin.2012.04.009>
- [40] I. Kyranou, S. Vijayakumar, M. S. Erden, Causes of performance degradation in non-invasive electromyographic pattern recognition in upper limb prostheses, *Frontiers in Neurorobotics* 12 (September) (2018) 1–22. doi:10.3389/fnbot.2018.00058.
- [41] S. Kanoga, A. Kanemura, H. Asoh, Are armband sEMG devices dense enough for long-term use?—Sensor placement shifts cause significant reduction in recognition accuracy, *Biomedical Signal Processing and Control* 60 (2020) 101981. doi:10.1016/j.bspc.2020.101981.  
URL <https://doi.org/10.1016/j.bspc.2020.101981>
- [42] Z. Li, X. Zhao, G. Liu, B. Zhang, D. Zhang, J. Han, Electrode shifts estimation and adaptive correction for improving robustness of sEMG-based recognition, *IEEE Journal of Biomedical and Health Informatics* 25 (4) (2021) 1101–1110. doi:10.1109/JBHI.2020.3012698.

## Supplementary Material

Table S1: Training time (mean  $\pm$  95% CI) for each regression algorithm using the multichannel linear descriptors-based block field method (MLD-BFM) feature ( $2 \times 2$  blocks, step size 1, 150 ms window, 1 sequence size).

Regression algorithm	Training time (s)
Ridge	$0.71 \pm 0.23$
Random Forest (RF)	$1.85 \pm 0.16$
k-Nearest Neighbors (KNN)	$1.99 \pm 0.23$
Lasso	$5.61 \pm 1.08$
Histogram Gradient Boost (HGB)	$4.31 \pm 0.10$
Multilayer Perceptron (MLP)	$15.52 \pm 0.59$

*Note:* All experiments were conducted using the scikit-learn library with CPU-only execution on a machine equipped with an Intel(R) Xeon(R) E-2246G CPU @ 3.60 GHz, 16 GB of RAM, running Windows 11 Pro.